Progress In Electromagnetics Research M, Vol. 111, 27–40, 2022

Comprehensive Analysis of a Novel Hybrid Excited Permanent Magnet Vernier Motor

Kai Zhang[1, *], Li Quan[1], and Xu Zhong[2]

Abstract—This paper proposes a hybrid excited permanent magnet vernier motor for low-speed and high-torque applications in electrical drive. Traditional PM vernier motors are with PM excitation field, and the air-gap magnetic field density is hard to adjust, which limit the wide speed range of PM motor. The hybrid excitation method is proposed in the PM vernier with excitation windings set in the region between modulation pole pieces. With the finite analysis method, the basic structure and working principle of the proposed motor are introduced, and the low-speed and high-torque characteristics with wide speed range are revealed. Then, the drive control system of the motor is designed and applied with the prototype motor. Finally, the experimental results verify the reliability and effectiveness of the design theory and simulation results.

1. INTRODUCTION

As the core power component in the electric drive, motor system has a direct influence on the entire performance. Due to the merits of high torque density, high power density, and high efficiency, permanent magnet (PM) motors have attracted much attention and have been widely applied in electric direct drive fields [1–3]. However, the excitation magnetic field of PM motors is produced with PMs, and the field is relatively static. The adjustment range of excitation magnetic field is limitedly controlled by flux weakening control based on vector control strategy, and the difficulty of wide range and efficient operation is increased. The hybrid excited motor adds a set of extra excitation winding to produce adjustable electric excitation magnetic field. The total excitation magnetic field can be flexibly adjusted after the superposition with PM field. Hence, high efficiency, high power density, and wide speed range can be simultaneously achieved [4–6].

At present, the common hybrid excited motor usually injects DC current in the excitation winding to produce electric excited magnetic field which is relatively static to excitation windings. Hence, the most direct hybrid excitation method is to employ the excitation winding in the rotor of the rotor-PM motor. This can lead to the same rotating speed of both the rotor and PMs. However, this method inevitably brings extra equipment including collector rings and electric brush. Hence, the hybrid excited motor with separate rotor magnetic flux was proposed. This method extended rotor iron core to provide the magnetic circuit for the axial excitation magnetic field and realized the brushless rotor type hybrid excitation motor with tangential magnetization [7]. A hybrid excitation motor with consequent-poles rotor was proposed for improvements, and further a hybrid excitation motor with segmented rotor structure was proposed [8]. The two sets of excitation winding were located in the stator iron core, and good voltage regulation capacity was achieved without collector rings and electric brush with the analyses from equivalent 2D magnetic circuit model. Contrarily, the stator-PM motor employs PMs in the stator to enhance the rotor robustness. The unique structure with both PMs and windings in stator

Received 28 February 2022, Accepted 7 May 2022, Scheduled 15 June 2022

* Corresponding author: Kai Zhang (2111807012@stmail.ujs.edu.cn).

[1] School of Electrical and Information Engineering, Jiangsu University, Zhenjiang 212013, China. [2] Jiangsu Automation Research Institute, Lianyungang 222000, China.

side provides convenience for adding excitation winding and realizing brushless hybrid excitation [9, 10]. However, this structure causes serious lack of space and suffers from concentrated heat sources.

On the other hand, it is one of the effective means to improve the operation efficiency of electric vehicles and reduce the complexity of the power system to realize the direct drive of electric vehicles by using hub motors. Due to the relatively low speed of the wheel, the field modulated PM motor based on the principle of field modulation and with the characteristics of low speed and high torque has become a research hotspot in this field [11–14]. Its potential applications mainly include electric vehicles, wind power generation, and other fields. However, similar to the ordinary PM motor, the field modulated PM motor still has the problems of difficult adjustment of excitation field and limited efficient operation range.

Combined with hybrid excitation and field modulated PM motor, a new hybrid excited PM vernier motor was proposed in [15], and its topology and basic electromagnetic characteristics were discussed and analyzed. By employing a set of three-phase secondary windings on the small teeth, a special dual AC winding structure was formed. In [16], a set of AC excitation winding was added to the alternating pole PM motor to achieve good magnetic field regulation performance, which further proves the feasibility of AC excitation scheme. The hybrid excited PM vernier motor not only inherits the characteristics of low speed and high torque of magnetic field modulation motor, which is suitable for direct drive occasions such as hub motor, but also can easily realize multi-mode operation such as field weakening speed expansion and double winding high torque by controlling the secondary winding current, which provides a beneficial idea for the wide speed range and efficient operation of electric vehicles [17–20]. However, in [15] and [16], the brushless double-fed machine and the hybrid excited machine were both theoretically analyzed without experimental results. Further, the flux-weakening performance analyses with mechanical characteristic curves were not discussed in [15]. And the modulation effect was not adapted in [16].

The main purpose of this paper is to propose a hybrid excited PM vernier motor for low-speed and high torque applications, and two sets of winding containing armature winding and excitation winding are adopted. With appropriate *d-q* axis current, different functions of improving torque and increasing speed with flux weakening can be realized separately. In Section 2, the structure and working principle of the proposed hybrid excited PM vernier motor are illustrated to indicate characteristics of both low-speed and high-torque and wide speed ranges. In Section 3, the corresponding electromagnetic performance is discussed and analyzed. At last, the experimental results verify the reliability and effectiveness of the design theory and simulation results.

2. STRUCTURE AND PRINCIPLE OF MOTOR

2.1. Motor Structure

Figure 1(a) shows the proposed hybrid excited PM vernier motor, and Figure 1(b) shows the BH curve of magnetic material. In the FEA model, the calculation period is 360 electric degrees, which means that the single step is calculated in static magnetic field with one certain rotor position. And the transient simulation is achieved by multi-steps of magnetic field calculation. It can be observed that the PMs are employed in the outer rotor, which owns a simple and robust structure. The PMs are magnetized radially with the opposite magnetization direction. For the inner stator, the stator structure is adopted with 6 main stator teeth, and the armature windings are set in the stator slots. Each stator tooth contains three modulation pole pieces, and the excitation windings are set in the region between modulation pole pieces. This operation makes full use of the space and effectively solves the conflict between the two sets of winding on the inner stator. The detailed key design parameters of the proposed motor are listed in the Table 1.

2.2. Basic Working Principle

Based on the air-gap magnetic field modulation theory [11], the relationship between pair of poles of winding, PMs, and number of modulation pole pieces of the PM motor with field modulation satisfies:

$$N_{st} = p_r \pm p_a = p_r \pm p_f \tag{1}$$

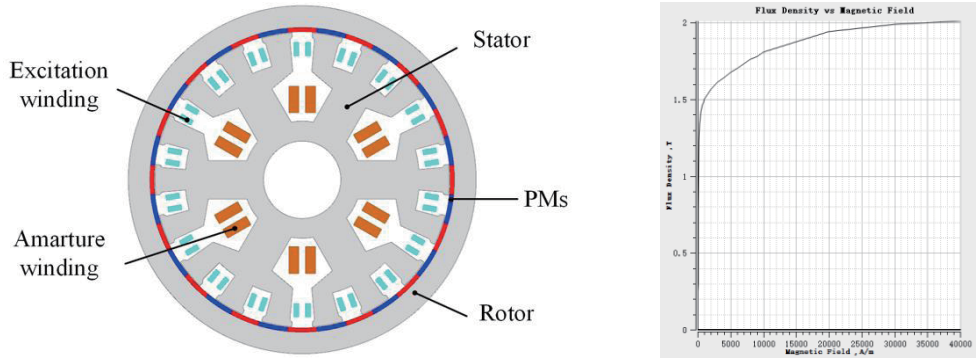

Figure 1. Structure. (a) Fractional-slot concentrated-winding PM machine. (b) B-H curve of iron material.

Table 1. Main motor specifications.

Items	Values
Rated power (kW)	5
Number of armature slots	6
Number of excitation slots	18
Pair of poles	16
Rotor outer diameter (mm)	208
Rotor inner diameter (mm)	182
Stator outer diameter (mm)	176
Stator inner diameter (mm)	48
Air-gap length (mm)	0.5
Length of modulation pole (mm)	22
Width of stator tooth (mm)	23
Length of stator tooth (mm)	22
Coil turns of armature winding	52
Coil turns of excitation winding	12
PM material	NdFe35
Iron core material	DW470_50
Thickness of PM (mm)	2.5

where N_{st} is the number of modulation pole pieces; p_r is the pair of poles of PMs; and p_a and p_f are the pair of poles of armature winding and excitation winding, respectively.

Ignoring the slot-opening, the equivalent air-gap MMF under PMs can be represented as Figure 2. By using Fourier decomposition method, the air-gap MMF F_{ag} can be expressed as:

$$F_{ag}(\theta, t) = \sum_{j=1,3,\ldots}^{+\infty} F_{agj} \cos[jp_r(\theta - \theta_0 - \omega_r t)] \tag{2}$$

where ω_r is the mechanical rotating speed; t is the time; θ and θ_0 are the current and initial position of rotor, respectivelyly; and air-gap MMF harmonic component F_{agj} can be expressed as:

$$F_{agj} = \frac{4F_{agm}}{j\pi} \sin(np_r l_1)$$

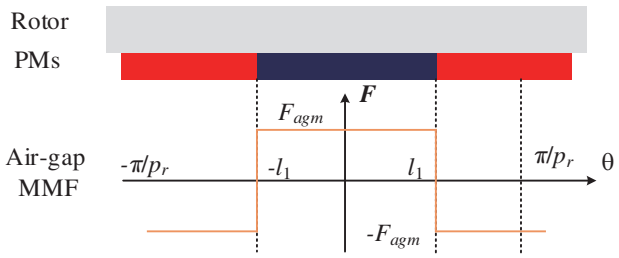

Figure 2. Equivalent air-gap MMF.

where l_1 is the half of the width of PM shown in Figure 2, and p_r is the number of pair of poles.

The arrangements of inner stator modulation pole pieces result in the change of the air-gap permeance. Figure 3 shows the air-gap permeance calculation model and the related parameters. Similar to the Fourier decomposition in (2), the air-gap permeance can be expressed as:

$$\lambda(\theta) = \lambda_0 + \sum_{m=1}^{+\infty} \lambda_m \cos(mN_{st}\theta) \tag{3}$$

with

$$\begin{cases} \lambda_0 = \dfrac{2\pi\lambda_{rl}}{N_{st}} + 2l(\lambda_{rh} - \lambda_{rl}) \\ \lambda_m = \dfrac{2(\lambda_{rh} - \lambda_{rl})}{mN_{st}} \sin(mN_{st}\theta) = \dfrac{2\lambda_{pp}}{mN_{st}} \sin(mN_{st}\theta) \end{cases} \tag{4}$$

where λ_0 is the DC component of the air-gap equivalent permeance; λ_m is the mth harmonic component; λ_{rh} and λ_{rl} are the peak and valley of the air-gap equivalent permeance respectively; λ_{pp} is the peak-to-peak value; l is half of the width of one tooth shown in Figure 3.

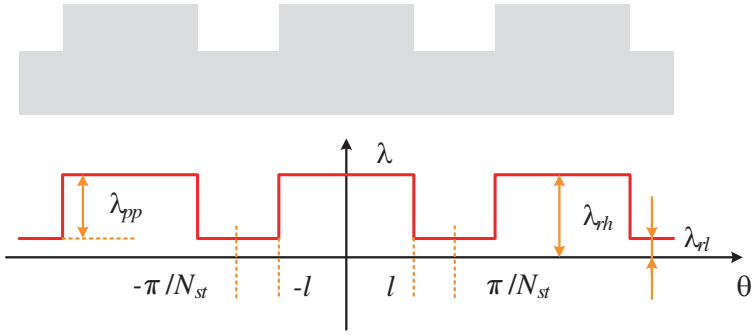

Figure 3. Equivalent air-gap permeance.

According to (2) and (3), the air-gap density of the hybrid excited PM vernier motor can be expressed as:

$$\begin{aligned} B_{ag}(\theta,t) &= F_{ag}(\theta,t)\lambda(\theta) \\ &= \sum_{j=1,3,\ldots}^{+\infty} \lambda_0 F_{agj} \cos[jp_r(\theta - \theta_0 - \omega_r t)] \\ &\quad + \sum_{j=1,3,\ldots}^{+\infty} \sum_{m=1}^{+\infty} \frac{F_{agj}\lambda_m}{2} \cos\left\{(jp_r + mN_{st})\left[\theta - \frac{jp_r(\theta_0 + \omega_r t)}{jp_r + mN_{st}}\right]\right\} \\ &\quad + \sum_{j=1,3,\ldots}^{+\infty} \sum_{m=1}^{+\infty} \frac{F_{agj}\lambda_m}{2} \cos\left\{(jp_r - mN_{st})\left[\theta - \frac{jp_r(\theta_0 + \omega_r t)}{jp_r - mN_{st}}\right]\right\} \end{aligned} \tag{5}$$

Table 2. Air-gap harmonic components.

Group	Order of harmonic components	Amplitude of harmonic components	Rotating speed of harmonic components	Initial position of harmonic components
1	p_r	$\lambda_0 F_{agj}$	w_r	θ_0
2	Jp_r+mN_{st}	$\lambda_m F_{agj}/2$	$jp_r w_r/(jp_r+mN_{st})$	$jp_r\theta_0/(jp_r+mN_{st})$
3	Jp_r-mN_{st}	$\lambda_m F_{agj}/2$	$jp_r w_r/(jp_r$-$mN_{st})$	$jp_r\theta_0/(jp_r+mN_{st})$

From (5), it can be concluded that three different harmonic components exist. The order, amplitude, rotating speed, and the initial position of the harmonic components are listed in Table 2. The first group harmonic component is generated by the interaction between the fundamental component of PMs and the DC component of air-gap permeance without modulation process. The second and third group harmonic components are modulated by the fundamental component of PMs through the first harmonic component of air-gap permeance. The second group harmonic owns more poles and lower rotating speed, while the third group harmonics owns fewer poles and higher rotating speed. Due to the low-speed and high-torque feature, the third group harmonics are utilized for application in direct drive system. The pair of poles p_{ef} and the rotating angle speed w_{ef} of the effective harmonic magnetic field can be expressed as:

$$p_{ef} = |p_r - N_{st}| \tag{6}$$

$$\omega_{ef} = \frac{p_r}{N_{st} - p_r}\omega_r = \frac{p_r}{p_{ef}}\omega_r = G_r\omega_r \tag{7}$$

2.3. Flux-Weakening Working Principle

To effectively reduce the air-gap magnetic field, the PM magnetic flux paths are required to be in the opposite direction from the electric exciting direction when the magnetic flux paths are the same. Figure 4 shows the flux paths with different excitation working modes. The electric exciting magnetic field can be strengthened by increasing the current of excitation winding, while the MMF amplitude of armature winding can be reduced by reversing electric excitation. The pair of poles of the excitation winding can be expressed with the harmonic order from effective components:

$$p_f = p_a = p_{ef} \tag{8}$$

The current frequency of excitation winding is required to keep pace with the PM magnetic field, which can be expressed as:

$$f_f = \frac{p_f\omega_f}{2\pi} = \frac{p_{ef}\omega_{ef}}{2\pi} = \frac{p_r\omega_r}{2\pi} \tag{9}$$

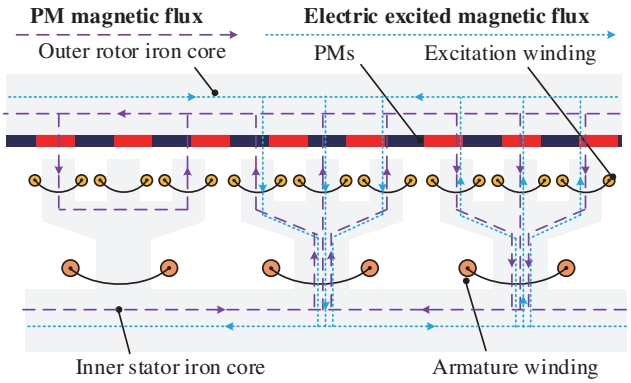

Figure 4. Flux path with different excitation working mode.

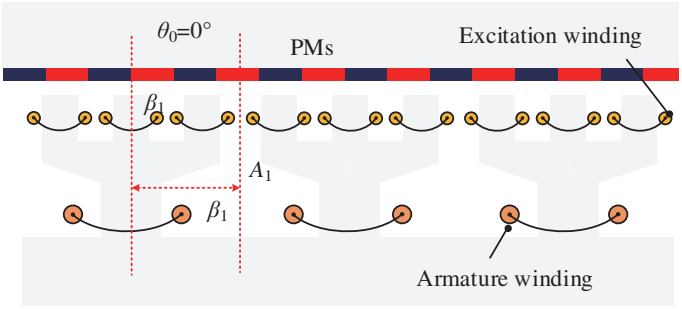

Figure 5. Relative position of PMs and windings.

Assuming that the initial position of PM is θ_0, the mechanical angle between the central axis of excitation winding and PM is β_1, which is shown in Figure 5. When the rotor is rotating, the magnetic flux phase θ_a of the armature winding can be expressed as:

$$\theta_a = p_f \theta_0 \tag{10}$$

$$\theta_f = \theta_a - p_f \beta_1 + \pi \tag{11}$$

2.4. Flux-Strengthening Working Principle

The electromagnetic torque of the PM motor can be expressed as the summary of three parts:

$$\begin{aligned} T_e &= T_{PM} + T_r + T_{cog} \\ &= \frac{3}{2} p_r \left[\psi_{PM} i_q + (L_d - L_q) i_d i_q\right] + T_{cog} \end{aligned} \tag{12}$$

where ψ_{PM} is the PM flux; i_q and i_d are the q-axis and d-axis components of winding current, respectively; L_q and L_d are the q-axis and d-axis components of inductance respectively.

In the proposed motor, L_q and L_d are basically the same, which means that the reluctance torque can be treated as 0. Then (12) can be transformed as:

$$T_e = T_{PM} = \frac{3}{2} p_r \psi_{PM} (i_{qa} + i_{qf}) \tag{13}$$

where i_{qa} and i_{qf} are the q-axis component of armature winding current and excitation winding current, respectively.

According to (13), when the armature winding and excitation winding are working with the q-axis currents simultaneously, the produced output torque of the motor is the summary of the two-part torque. This feature can improve the electromagnetic torque. For illustration, the air-gap density of the proposed motor is analyzed. First, the PMs from the motor are removed in the simulation, and Figure 6 compares three working modes with the armature winding alone, the excitation winding alone, and the dual windings. It can be seen from Figure 6(a) that three waveforms basically achieve a good agreement with each other with some minor discrepancy on the amplitude. The harmonic analyses from Figure 6(b) show that the amplitude of armature winding working alone is 0.2 T for the 2nd harmonic. The amplitude of excitation winding working alone is 0.13 T while the dual windings is 0.32 T. These results show that the amplitude of dual winding working mode is approximate to the superposition of the amplitudes of harmonic components produced by the two sets of solo working windings.

3. RESULTS AND VERIFICATIONS

Generally speaking, the torque is generated by applying q-axis current to the armature winding, and the field weakening is realized by applying d-axis current to the excitation winding of the auxiliary winding. The rotation control of DQ axis is realized by controlling the positive and negative directions of DQ axis. The back-EMF, inductance, and torque of Figures 7–9 are calculated by finite element analysis software

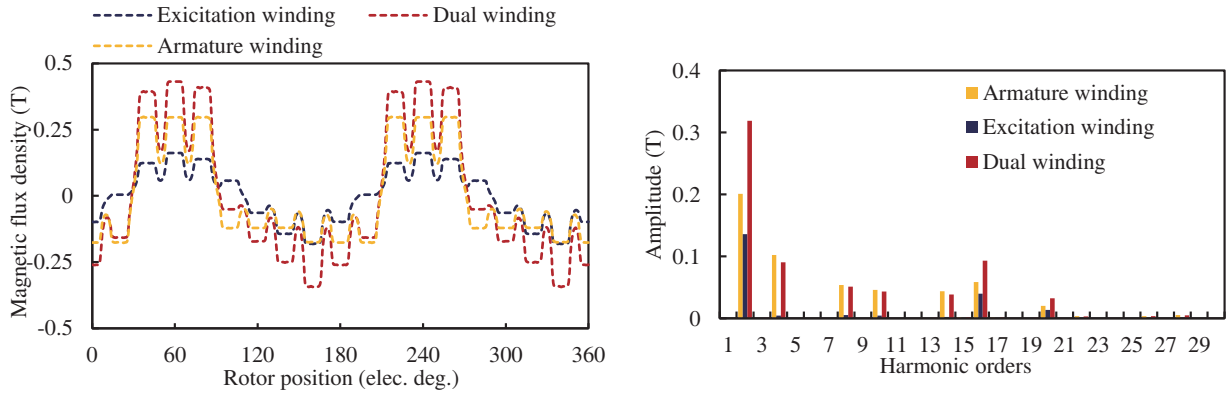

Figure 6. Air-gap magnetic flux density under different winding function. (a) Density waveform. (b) Harmonic analysis.

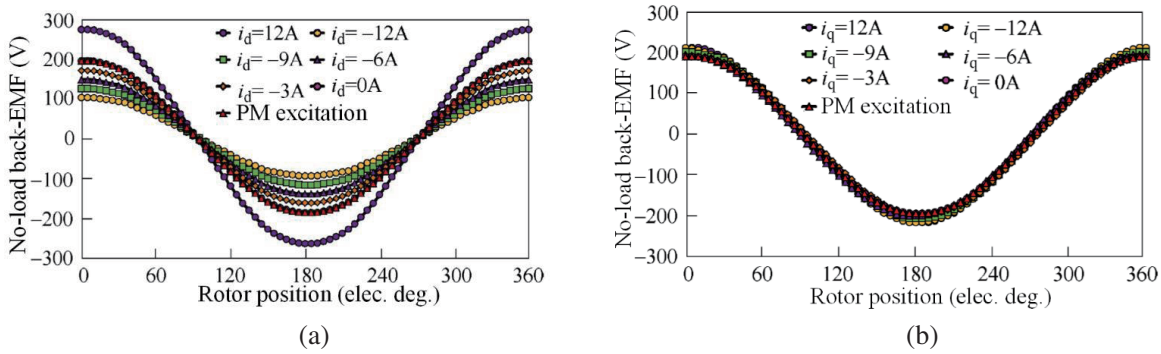

Figure 7. No-load back-EMF in phase A under different excitations. (a) id injected in excitation winding. (b) iq injected in excitation winding.

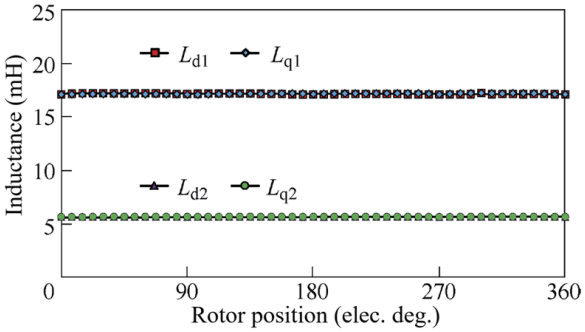

Figure 8. Inductance waveforms in *d*-*q* axis.

to guarantee the high analyzing accuracy instead of mathematic equations. The analytical equations in Section 2 are used to guide the direction of motor design. For instance, the modulation theory in (8) expresses the basis of motor operation, which is important to guarantee the stable application. Meanwhile, due to the saturation of proposed motor, analytical results are not acceptable because they ignore the permeability of iron core. FE simulation is not only the verification of analytical theory, but also a guarantee of high accuracy. Figure 7 shows the no-load back-EMF of the armature winding when the PMs are excited, and the *d*-axis and *q*-axis currents of different amplitudes are applied to the excitation winding. Because the motor is operated based on the principle of magnetic field modulation,

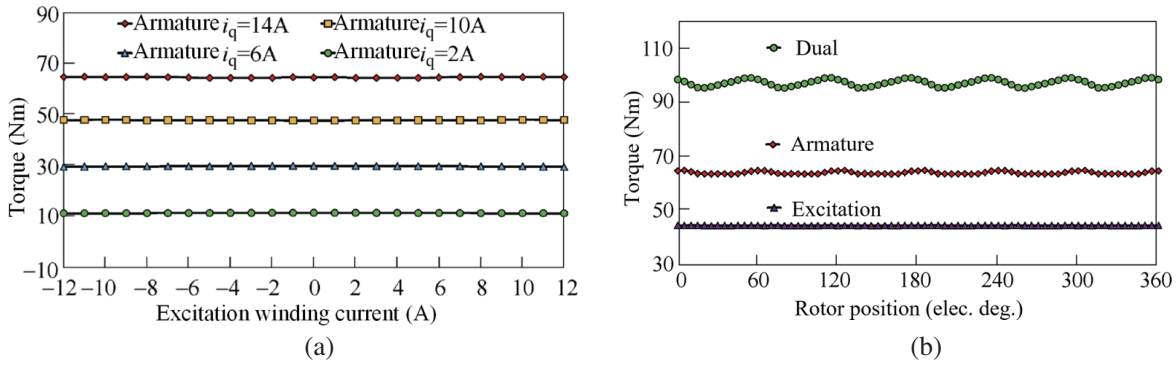

Figure 9. Torque waveforms in different working mode. (a) Flux weakening. (b) Dual winding.

the induced EMF is very sinusoidal. Figure 7(a) compares the back EMF of the motor when different d-axis currents are injected to the excitation winding. The induced EMF increment of the main winding is almost linear with the current of the excitation winding, and the magnetic weakening coefficient is defined as:

$$\gamma = \frac{e_{PM} - e^{-}}{e_{PM}} \tag{14}$$

where e_{PM} and e^{-} are the peak values of no-load back-EMF under PM excitation and minimum flux weakening, respectively. When d-axis flux weakening current is applied to the excitation winding, the flux weakening rate can reach 48.16%. Figure 7(b) compares the motor back EMF when different q-axis currents are applied, and the excitation winding is used as the armature winding. The induced EMF of the main winding has no obvious change, which further verifies that the proposed motor can effectively work in the flux weakening mode with high speed and double winding mode with large torque when the excitation winding is used as the armature winding.

The inductances of d-axis and q-axis are shown in Figure 8. It can be noticed that the inductances of d-axis and q-axis of two sets of windings do not change with the rotor position with $L_{d1} = L_{q1}$, $L_{d2} = L_{q2}$. It should be noted that there is a strong mutual inductance between the two windings because the two sets of windings are used in the motor. However, the mutual inductance will not affect the output torque. The torque waveforms under different modes are shown in Figure 9. Figure 9(a) shows the torque waveform changing with i_q in armature winding when different flux weakening currents are applied to the excitation winding. It can be seen that the torque increases linearly with the amplitude of the i_q in armature winding, but not affected by the i_d in excitation winding. Namely, the torque of the motor will not be reduced due to the field weakening operation based on the excitation winding, but the voltage at both ends of the armature winding can be effectively controlled with the help of the excitation magnetic field of the excitation winding, as shown in Figure 7(a). This feature is superior to the ordinary PM motor and the existing hybrid excited motor. In addition, for the same reason, the proposed motor does not use the magnetization operation based on the excitation winding, but adopts dual winding operation mode in which the armature winding and excitation winding are both armature windings, so as to meet the requirements of high torque condition of electric vehicles. Figure 9(b) shows the electromagnetic torque waveform when the rated i_q is applied to two sets of windings, respectively. Figure 8 shows the DQ axis inductance of the motor, in which L_{d1} and L_{d2} are the main and auxiliary winding d-axis inductance, L_{q1} and L_{q2} are the main and auxiliary winding q-axis inductances. As can be seen from Figure 9(a), when the field weakening stage is in, that is, the Id current of the excitation winding is -12 A$\sim$12 A, the increase of the armature winding current i_q will increase the average torque of the motor, and the torque is basically not affected by the i_d. At the same time, it can be seen from Figure 9(b) that when the output is in the maximum torque state, and the double windings are connected with the same phase i_q current at the same time, the total torque is basically the sum of the torques generated by the two sets of windings respectively. The average torques are 63.65 Nm and 44.01 Nm with only the armature winding or the excitation winding. The average torque with two windings is 97.18 Nm which is the sum of the electromagnetic torque generated in the double winding

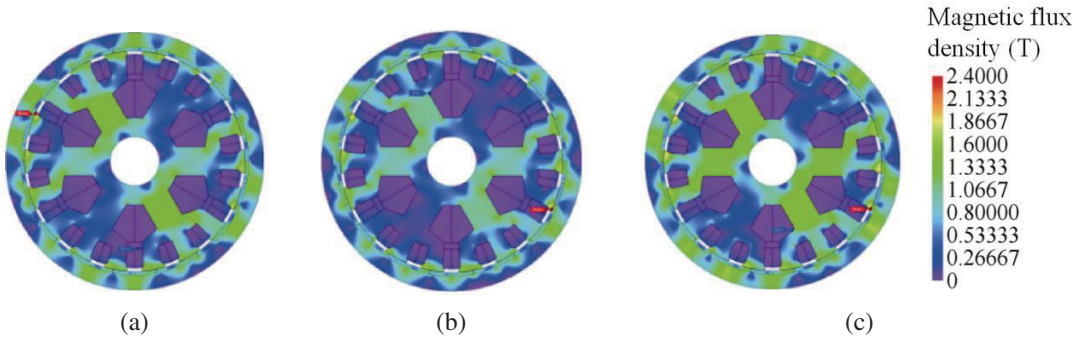

Figure 10. Electromagnetic cloud map of motor under different full-load operation conditions. (a) Mode I. (b) Mode II. (b) Mode III.

mode. The torque value is almost the same as the summary when the two windings act respectively. The slight difference is caused by the local saturation of the core. Figure 10 shows the flux density cloud map of the motor at full load under different working conditions. It can be seen that the flux density of mode I and mode III is more saturated than that of mode II, but both are within a reasonable range. Mode I is Amature mode; mode II is Excitation mode; and mode III is dual mode. According to the torque shown in Figure 9(b), the capacities of three different modes are indicated, which means that the excitation mode has the lowest saturation while the dual mode has the highest saturation.

Figure 11 shows the mechanical characteristic curve of the motor. The flux weakening curve shown in Figure 11 meets the limits of voltage limit circle and current limit circle, which are analyzed and calculated by finite element software.

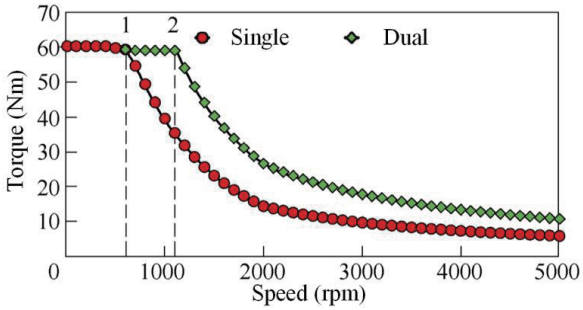

Figure 11. Mechanical characteristic curves of the proposed motor.

Therefore, under full load working condition, the maximum speed is limited by the voltage limit circle, which is the maximum speed that can be obtained by adjusting the current angle under this torque. In Figure 11, it can be clearly seen that when the speed is 5000 rpm, the torque of the double winding motor is twice that of the single winding. Similarly, the double windings will obtain a higher maximum speed under the same torque. For ordinary permanent magnet motor, its weak magnetic performance is similar to that of single winding, and the difference is that there is no auxiliary excitation winding. The criteria of voltage limit circle and current limit circle for the flux weakening operation are expressed as:

$$(i_d + \psi_f/L_0)^2 + i_q^2 \leq [U_{\lim}/(\omega_e L_0)]^2 \tag{15}$$

Among them, Point 1 and Point 2 correspond to the full load point of single winding motor and dual winding motor, respectively. It can be found that the maximum output torque is about 60 Nm, and the base speed is 600 rpm under the single winding operation condition. The performance of the motor shown in Figure 7(a) is basically close to that of ordinary SPM motor, but its advantage lies in the field weakening performance of multiple windings. As shown in Figure 11, when the motor adopts double

winding operation condition, the field weakening performance of the proposed motor can be greatly improved. When the excitation winding is added, the basic speed of the motor increases to 1100 rpm, and the torque between Point 1 and Point 2 remains unchanged, which effectively expands the speed range of the motor.

4. EXPERIMENTS

In order to verify the reliability of theoretical analysis and simulation, the prototype is built as shown in Figure 12, and a series of experimental tests are carried out on the prototype. The driving system consists of control and driving part, which are DSP, CPLD and MOSFET driving, respectively. The DQ axis current is decomposed by the mathematical model written in advance in DSP, and the three-phase current is separated by Parker Clark transform to extract the DQ axis current. Figure 12(a) shows the cross section of the stator. Figure 12(b) shows the stator assembly. Figure 12(c) shows the experimental platform, and Figure 12(d) shows the experimental system. The manufacturing factory uses wire-electrode cutting to process silicon steel sheets and stack out the stator and rotor. Further, they magnetize and cut the rare earth materials, process the stator casing and end cover at the same time, and finally assemble the motor. In a word, compared with the general permanent magnet synchronous motor processing, it is basically the same without additional special treatments. Figure 13 shows the general block diagram of motor system control. The system includes an outer speed loop, four inner current loops, a control algorithm module, and an interval judgment module. The control algorithm module includes the motion control strategy of each area of the motor, and the area judgment module, according to the torque T_e and speed fed back by the motor ω_r to judge the motor movement section, gives the AC-DC axis current of main winding and auxiliary winding to control the motor in different areas. The speed loop forces the motor speed to follow the given speed well, and the current loop forces the AC-DC axis current to follow the given speed, which enhances the dynamic performance of the motor.

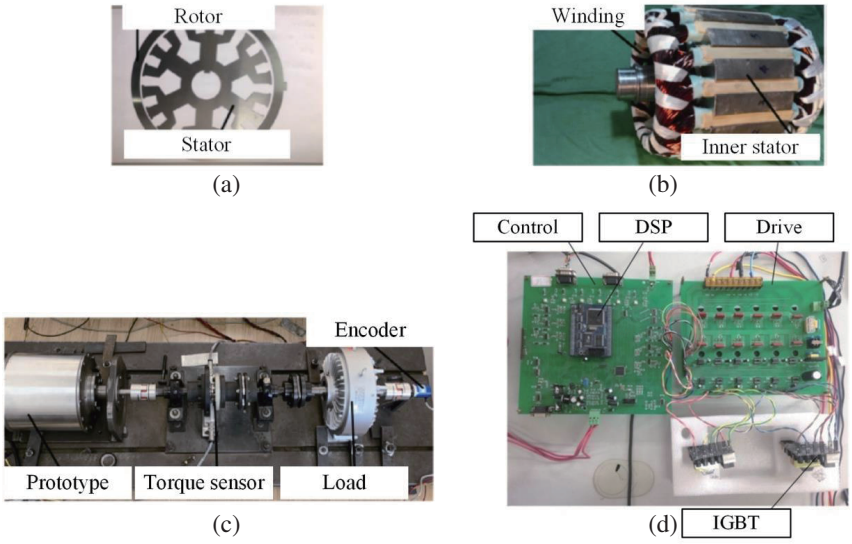

Figure 12. Prototype and text platform of the hybrid excited PM vernier motor. (a) Stator. (b) Stator assembly. (c) Experimental platform. (d) Control system.

The measured no-load back-EMF waveforms under PM excitation are shown in Figure 14. Figure 14(a) and Figure 14(b) show the no-load back-EMF of the armature winding and the excitation winding of when the speed is 300 rpm. It can be seen that the measured waveforms are sinusoidal and symmetrical. The peak values of the no-load back-EMF of the armature winding and excitation windings are about 94 V and 73 V, which are 97.7% and 97.3% of the finite element simulation in Figure 14(c), respectively.

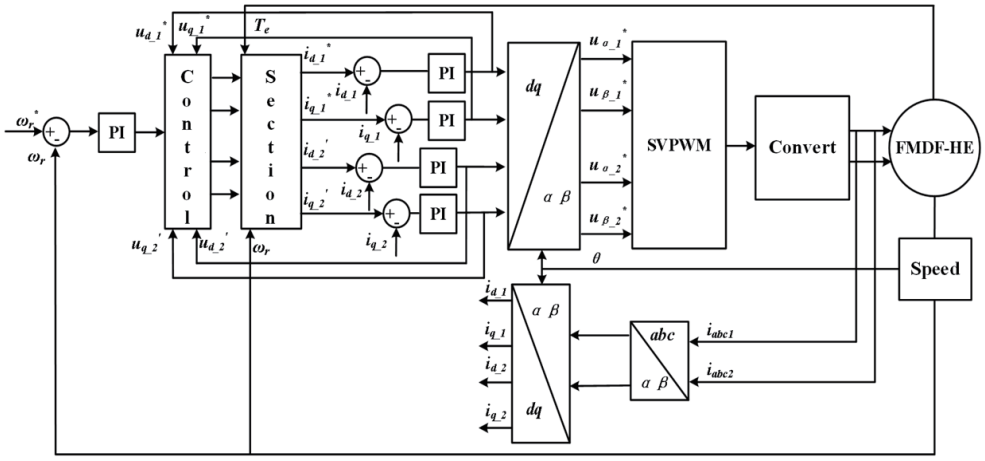

Figure 13. General block diagram of motor system control.

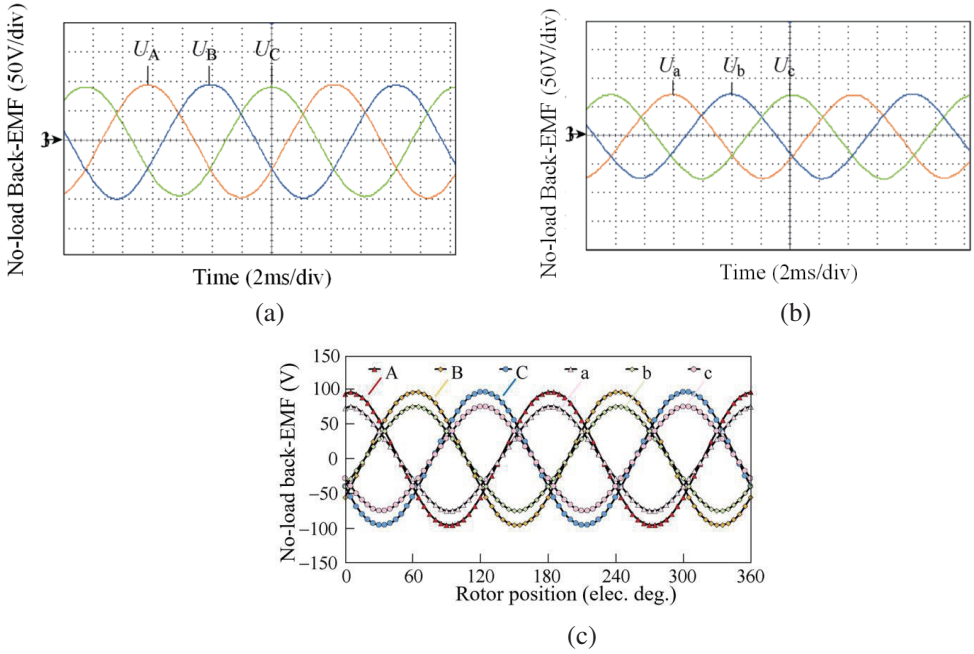

Figure 14. Measured no-load back-EMF. (a) Armature winding. (b) Excitation winding. (c) Simulated results.

Actually, even though the experiments are carried out with voltage fed, the simulation is based on the sinusoidal current fed. The reason is that the rated-current is the fundamental part of motor-driving and using current injection which is the most common way to estimate the magnetic performance. Hence, the simulation is ideal without the coupling calculation. But the experiment is operated with the same sinusoidal winding current, which is very appropriate to the simulation. When the excitation winding is excited, the measured no-load back-EMF of the armature winding is shown in Figure 15. Figure 15(a) and Figure 15(b) show the no-load back-EMF of the armature winding when the motor speed is 100 rpm, and $i_{d2} = \pm 12$ A is applied to the excitation winding. It can be seen that before the current is applied to the excitation winding, the no-load back-EMF of the armature winding is 31 V, which is consistent with the finite element simulation results. When $i_{d2} = 12$ A is applied to the excitation winding, the motor is in the magnetization increasing state, which makes the no-load back-EMF of the main winding increase to 42 V. When $i_{d2} = -12$ A is applied to the excitation winding, the motor is in the flux weakening state, and the no-load back-EMF of the main winding decreases to 17 V, which are 92.9% and 102.3%

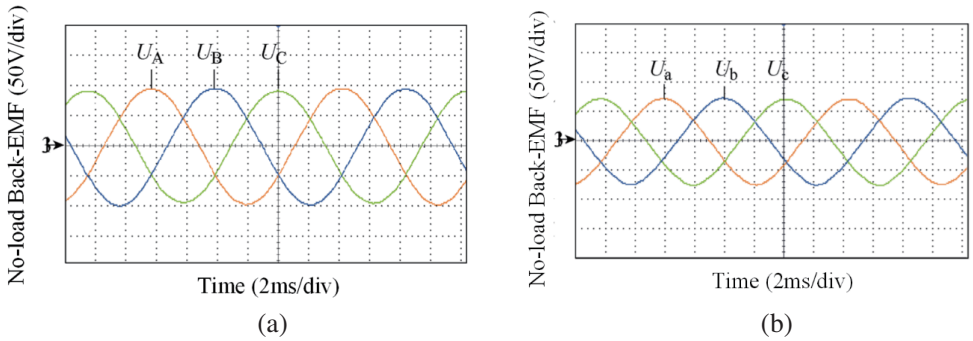

Figure 15. Measured no-load back-EMF waveforms of armature winding with different excitations. (a) i_d of excitation winding turn to 12 A from 0 A. (b) i_d of excitation winding turn to −12 A from 0 A.

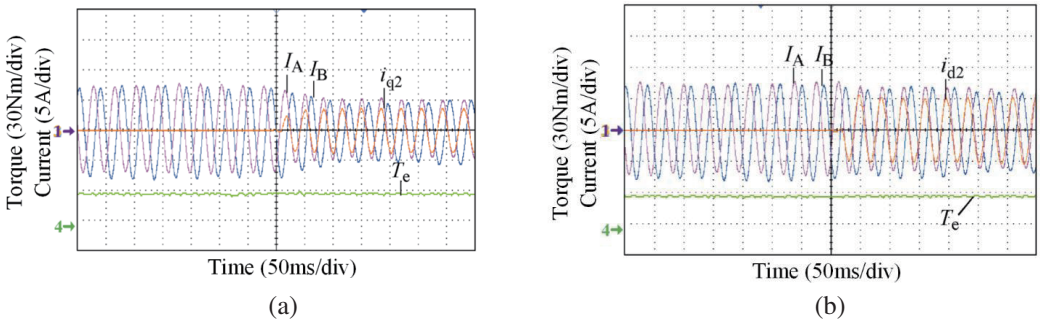

Figure 16. Current of armature winding and torque waveforms with and without excitation winding current. (a) iq of excitation winding is injected. (b) id of excitation winding is injected.

of the finite element simulation results, respectively.

Figure 16 shows the waveform of current and torque of armature winding when the sudden current is applied to excitation winding. Figure 16(a) and Figure 16(b) show the torque of the motor and the current waveforms of the armature winding and excitation winding respectively when the armature winding is driven respectively, and the speed is set to 100 rpm under the condition of constant load torque. It can be seen that the three-phase current peak value of the armature winding is 7 A when the armature winding is driven alone. When $i_{q2} = 3$ A is suddenly added to the excitation winding, the three-phase current peak value of the armature winding drops to 5 A, which indicates that i_{q2} of the excitation winding provides a certain output torque. At this time, the total output torque of the motor is the sum of the output torque of the armature winding and excitation winding. However, when $i_{d2} = 5$ A is suddenly added to the excitation winding, there is no obvious change in the peak current of the armature winding after the injection, which indicates that the i_{d2} component of the excitation winding cannot provide torque and has no effect on the torque, which is consistent with the theoretical analysis and finite element simulation results.

5. CONCLUSION

In this paper, a novel hybrid excited PM vernier motor for low-speed and high torque applications in electrical drive is proposed. The hybrid excitation method is proposed in the PM vernier with two sets of winding containing armature winding and excitation winding adopted. The excitation windings are set in the region between modulation pole pieces. With appropriate *d-q* axis current, different functions of improving torque and increasing speed with flux weakening can be realized respectively. Based on the finite analysis method, the basic structure and working principle of the proposed motor are introduced, and the low-speed and high-torque characteristics with wide speed range are revealed. Then, the drive control system of the motor is designed and applied with the prototype motor. Finally, the experimental results verify the reliability and effectiveness of the design theory and simulation results.

REFERENCES

1. Petkar, S.-G., K. Eshwar, and V.-K. Thippiripati, "A modified model predictive current control of permanent magnet synchronous motor drive," *IEEE Transactions on Industrial Electronics*, Vol. 68, No. 2, 1025–1034, 2021.
2. Arafat, A.-K.-M. and S. Choi, "Optimal phase advance under fault-tolerant control of a five-phase permanent magnet assisted synchronous reluctance motor," *IEEE Transactions on Industrial Electronics*, Vol. 65, No. 4, 2915–2924, 2018.
3. Chen, Y., X. Zhu, L. Quan, Z. Xiang, Y. Du, and X. Bu, "A V-shaped PM vernier motor with enhanced flux-modulated effect and low torque ripple," *IEEE Transactions on Magnetics*, Vol. 54, No. 11, 2018.
4. Shen, Y. and Q. Lu, "Design and analysis of linear hybrid-excited slot permanent magnet machines," *IEEE Transactions on Magnetics*, Vol. 54, No. 11, 2018.
5. Hua, H. and Z.-Q. Zhu, "Novel hybrid-excited switched-flux machine having separate field winding stator," *IEEE Transactions on Magnetics*, Vol. 52, No. 7, 2016.
6. Zheng, M., Z.-Q. Zhu, S. Cai, H.-Y. Li, and Y. Liu, "Influence of magnetic saturation and rotor eccentricity on back EMF of novel hybrid-excited stator slot opening permanent magnet machine," *IEEE Transactions on Magnetics*, Vol. 54, No. 11, 2018.
7. Liu, Y., Z. Zhang, C. Wang, W. Geng, and H. Wang, "Electromagnetic performance analysis of a new hybrid excitation synchronous machine for electric vehicle applications," *IEEE Transactions on Magnetics*, Vol. 54, No. 11, 2018.
8. Tapia, J.-A., F. Leonardi, and T.-A. Lipo, "Consequent pole permanent magnet machine with extended field weakening capability," *IEEE Transactions on Industry Applications*, Vol. 39, No. 6, 1704–1709, 2003.
9. Lin, N., D. Wang, K. Wei, et al., "Mathematical model and equivalent analysis of a novel hybrid excitation synchronous machine," *Transactions of China Electrotechnical Society*, Vol. 32, No. 3, 149–156, 2017.
10. Du, Y., C. Zhang, X. Zhu, et al., "Principle and analysis of doubly salient PM motor with π-shaped stator iron core segments," *IEEE Transactions on Industrial Electronics*, Vol. 66, No. 3, 1962–1972, 2019.
11. Cheng, M., P. Han, and W. Hua, "General airgap field modulation theory for electrical machines," *IEEE Transactions on Industrial Electronics*, Vol. 64, No. 8, 6063–6074, 2015.
12. Du, Y., et al., "Design and analysis of linear stator permanent magnet vernier machines," *IEEE Transactions on Magnetics*, Vol. 47, No. 10, 4219–4222, 2011.
13. Xu, L., G. Liu, W. Zhao, J. Ji, and X. Fan, "High-performance fault tolerant halbach permanent magnet vernier machines for safety-critical applications," *IEEE Transactions on Magnetics*, Vol. 52, No. 7, 2016.
14. Ching, T.-W., K.-T. Chau, and W. Li, "Power factor improvement of a linear vernier permanent-magnet machine using auxiliary DC field excitation," *IEEE Transactions on Magnetics*, Vol. 52, No. 7, 2016.
15. Liu, X., X. Zhong, Y. Du, et al., "A new magnetic field modulation type of brushless double-fed machine," *IEEE Transactions on Applied Superconductivity*, Vol. 28, No. 3, 2018.
16. Li, J. and K. Wang, "A parallel hybrid excited machine using consequent pole rotor and AC field winding," *IEEE Transactions on Magnetics*, Vol. 55, No. 6, 2019.
17. Tarimer, I., "Investigation of the effects of rotor pole geometry and permanent magnet to line start permanent magnet synchronous motor's efficiency," *Elektronika Ir Elektrotechnika*, Vol. 90, No. 2, 67–72, 2009.
18. Tarimer, I. and R. Gurbuz, "Sizing of electrical motors for gearless and directly stimulating applications," *Elektronika Ir Elektrotechnika*, Vol. 84, No. 4, 21–26, 2008.
19. Tarimer, I., A. Akpunar, and R. Gurbuz, "Design of a direct sliding gearless electrical motor for an ergonomic electrical wheelchair," *Elektronika ir Elektrotechnika*, Vol. 83, No. 3, 75–80, 2008.

20. Tarimer, I. and A. Akpunar, "Designing an ergonomic electric wheelchair in which is settled gearless and direct drive electric motor," *3rd Automation Symposium*, 21–25, Pamukkale University, Denizli, November 11–12, 2008.